Journal of Inorganic and Organometallic Polymers and Materials (2022) 32:1840–1852
https://doi.org/10.1007/s10904-022-02242-y

Preparation of Dual Z-scheme $Bi_2MoO_6/ZnSnO_3/ZnO$ Heterostructure Photocatalyst for Efficient Visible Light Degradation of Organic Pollutants

Yuanyingxue Gao[1] · Li Li[1,2] · Wenlin Zu[1] · Yingru Sun[1] · Jiahui Guan[2] · Yanzhen Cao[1] · Haixia Yu[1] · Wenzhi Zhang[1]

Received: 17 November 2021 / Accepted: 28 January 2022 / Published online: 10 February 2022

Abstract

In this study, a double Z-type $Bi_2MoO_6/ZnSnO_3/ZnO$ heterostructure photocatalyst was prepared by hydrothermal method to realize effective charge separation and improve photocatalytic activity. The synthesized samples were carefully examined by X-ray photoelectron spectroscopy, X-ray diffraction, scanning electron microscope, high-resolution transmission electron microscopy, photoluminescence (PL), and other analytical techniques. Meanwhile, the photocatalytic performance was further evaluated by multi-mode photocatalytic degradation with crystal violet (CV). The results show that the composite material has a relatively homogeneous cubic structure in size and shape. In the cubic structure, a heterogeneous structure exists between Bi_2MoO_6, $ZnSnO_3$ and ZnO. Simultaneously, the dramatic changes in physical morphology, such as the specific surface area and particle size of the composites, led to a series of unique properties, such as a significant climb in light absorption properties and superior photocatalytic activity. In addition, compared to ZnO, Bi_2MoO_6 and $ZnSnO_3/ZnO$, the $Bi_2MoO_6/ZnSnO_3/ZnO$ composite material shows lower PL intensity, smaller arc radius, and stronger photocurrent response. Meanwhile, $Bi_2MoO_6/ZnSnO_3/ZnO$ shows higher photocatalytic efficiency for CV and tetracycline hydrochloride (TC), and maintains good stability after 3 cycles of photodegradation experiments. Based on experimental results, the existence of heterojunctions between ZnO, $ZnSnO_3$ and Bi_2MoO_6 and the possible photocatalytic mechanism for the degradation of CV by dual Z-scheme composites are proposed. In conclusion, this study provides a feasible strategy for the photocatalytic degradation of organic pollutants by introducing $ZnSnO_3$ and Bi_2MoO_6 to successfully construct composite catalysts with dual Z-scheme heterostructures.

Keywords Hydrothermal method · Heterojunction · Dual Z-scheme · $Bi_2MoO_6/ZnSnO_3/ZnO$ · Photocatalysis · Crystal violet · Degradation mechanism

1 Introduction

In the last decades, with the rapid industrial development, population explosion and abuse of chemical disposal methods large-scale environmental pollution has been caused and serious health problems have been brought to mankind [1, 2]. Among all kinds of wastewaters, the wastewater from the dye industry is one of the main causes of environmental pollution, especially water pollution [3–5]. Approximately 650,000 tons of different dyes are used in the production of textiles every year [6–9]. Pretreatment of organic wastewater before discharge is very necessary because it has some characteristics such as nonbiodegradability and carcinogenicity [10].

Semiconductor photocatalysts have attracted extensive attention due to their wide application scopes in the direct elimination of harmful environmental pollutants, such as chromium, dyes, drugs, and other heavy metals using solar energy [11, 12]. A series of wide band gap semiconductors with excellent performance are widely used in various fields of photocatalytic applications, including ZnO and TiO_2 [13–15]. Light capture, charge separation and migration

✉ Li Li
qqhrll@163.com; qqhrlili@126.com

✉ Wenzhi Zhang
zhangwenzhi@qqhru.edu.cn

[1] College of Chemistry and Chemical Engineering, Qiqihar University, Qiqihar 161006, People's Republic of China

[2] College of Materials Science and Engineering, Qiqihar University, Qiqihar 161006, People's Republic of China

are considered to be the most complex and key factors to determine the efficiency of photocatalytic reaction. However, these broadband gap photocatalysts are usually excited only by ultraviolet light and have high photogenerated electron–hole pairs recombination rate, which greatly limits their application [16, 17]. In order to solve this phenomenon, researchers have found that Z-scheme photocatalysts inspired by natural photosynthesis have great potential for achieving high photocatalytic performance [18]. Due to the unique charge transfer mechanism, Z-scheme photocatalyst can separate photo-generated charge effectively, therefore it displays strong reduction and oxidation ability at the same time [19].

Zinc stannate ($ZnSnO_3$), as an attractive multifunctional material, has been applied in many fields such as gas sensor, photo-electrochemical device and photocatalyst [20]. Meanwhile, its face centered perovskite where each ZnO_6 octahedron shares a face with SnO_6 octahedron exerts remarkable role in the optical properties [21]. At the same time, when the material reaches the nano scale, the increase of specific surface area increases the migration rate of photogenerated electrons from the bulk phase to the surface, and then the probability of electron–hole pairs recombination is further reduced, which effectively improves the quantum yield and the reaction activity of photocatalyst. As is known, the photocatalytic performance is strongly related to the surface morphologies of materials, which the uniform morphology and moderate size contribute to the enhanced photocatalytic activity. Therefore, different morphologies of $ZnSnO_3$ including hollow spheres [22], cubic crystallites [23], etc. Although $ZnSnO_3$ shows amazing potential in the field of photocatalysis, the utilization of $ZnSnO_3$ under visible light irradiation is still a long-term challenge.

To address the drawbacks associated with conventional semiconductor photocatalysts, recent studies have focused on the use of narrow Eg ternary metal oxides as more efficient and alternative visible light-active photocatalytic systems for environmental remediation and energy production under solar light [24]. Bi(III)-containing oxides have attracted much attention in the field of photocatalysis due to their better intrinsic properties and special layered structures [25, 26]. Remarkably, bismuth molybdate (Bi_2MoO_6) is composed of alternating perovskite $[Bi_2O_2]^{2+}$ and (MoO_4^{2-}) layers, which gives it a manageable morphology and a suitable band gap value (2.5–2.7 eV) to capture visible light [27, 28]. Though a narrow Eg allows efficient absorption of visible light, it also often leads to certain undesired characteristics such as faster recombination rate of charge carriers and hence low photoactivity of ternary metal oxides, including Bi_2MoO_6 [29]. Therefore, the formation of semiconducting heterojunctions, especially in Z-scheme configuration [30], has been regarded as an efficient and important strategy to reduce charge-carriers recombination rate and improve absorption and the site effective photoactivity. However, in view of the exponential growth of the published research on the application of ZnO based Z-scheme heterojunction to the photocatalytic degradation of pollutants, to our knowledge, there is no article on the theme of double Z-type Bi_2MoO_6/$ZnSnO_3$/ZnO proposed in this paper.

In this paper, a double Z-type heterostructure composite photocatalyst Bi_2MoO_6/$ZnSnO_3$/ZnO with visible light response was prepared by hydrothermal method. Meanwhile, the morphology, crystal structure, element valence and photoelectrochemical properties of the novel composite photocatalyst were analyzed and characterized. In addition, the photocatalytic degradation efficiency of crystal violet (CV) and tetracycline (TC) under visible light irradiation was effectively evaluated. Finally, the reaction mechanism of the synthesized double Z-type photocatalyst was further analyzed. This study provides insights into the successful construction of double Z-type heterojunction, enhancing the light absorption capacity and promoting the effective separation of photogenerated electron–hole pairs, so as to accelerate the process of photocatalytic reaction.

2 Experimental Part

The monomers zinc oxide and $ZnSnO_3$/ZnO were synthesized by a simple hydrothermal method as detailed in the supporting information.

Synthesis of Bi_2MoO_6/$ZnSnO_3$/ZnO composite: 0.873 g bismuth nitrate pentahydrate and 0.218 g sodium molybdate were dissolved in 20 mL of ethylene glycol, and $ZnSnO_3$/ZnO was further dissolved in 10 mL ethylene glycol; the two solutions were mixed after stirring well. After complete dissolution, the mixed solution was poured into a Teflon autoclave and heated in an oven at 160 °C for 6 h. The product was washed several times with deionized water and ethanol, followed by drying at 60 °C for 12 h to obtain the Bi_2MoO_6/$ZnSnO_3$/ZnO composite (The molar concentration ratio of Bi_2MoO_6:$ZnSnO_3$:ZnO is 0.9:1.2:2.9).

3 Results and Discussion

3.1 XRD Analysis

The crystal structures of the synthesized composites were analyzed using X-ray diffraction (XRD). As shown in Fig. 1, the pure ZnO has diffraction peaks at 31.8°, 36.2°, 47.5°, 56.6°, and 68.2°, corresponding to the (100), (102), (110), (103), and (112) crystal planes, respectively, indicating that the ZnO in the composites belongs to the hexagonal wurtzite structure (JCPDS#36-1451). The diffraction peaks of this sample are sharp, indicating that the as-synthesized ZnO has excellent

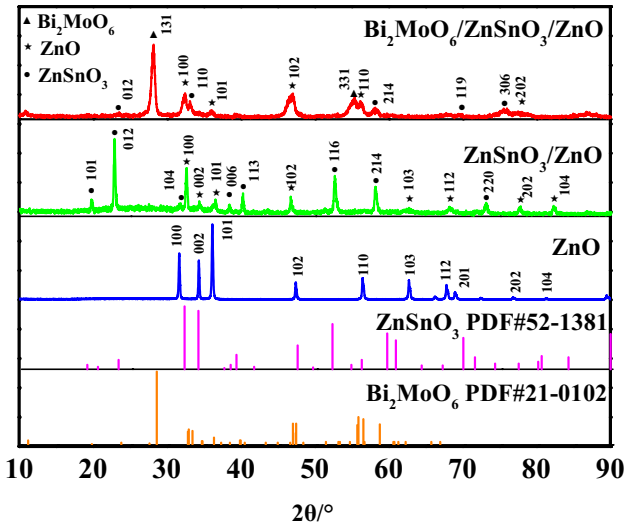

Fig. 1 XRD spectra of ZnO, $ZnSnO_3$/ZnO and Bi_2MoO_6/$ZnSnO_3$/ZnO

crystallinity. The diffraction peaks of the composites at 28.3° and 55.4° correspond to the (131) and (331) crystal planes of Bi_2MoO_6, respectively (JCPDS#21-0102). The diffraction peaks of the composites are at 23.1°, 33.9°, 59.5°, and 89.7°, corresponding to the (012), (110), (214), and (309) crystal planes of $ZnSnO_3$ (JCPDS#52-1381), respectively. Moreover, these diffraction peaks of this composite are sharp without redundant hetero peaks, indicating that the crystallinity of the as-synthesized sample is excellent, and no impurities were introduced. Compared with the $ZnSnO_3$/ZnO composite, the intensity and type of the diffraction peak of Bi_2MoO_6/$ZnSnO_3$/ZnO composite are slightly weakened due to the reduced crystallinity of the composite after secondary hydrothermal. In addition, the diffraction peaks of the Bi_2MoO_6/$ZnSnO_3$/ZnO composite are slightly wider than those of the other materials, suggesting that the as-synthesized composite has smaller grain sizes, which may be the result of the secondary hydrothermal.

The average crystallite size of each material was calculated by Scherrer's equation (Eq. 1), and the results are shown in Table 1.

$$d = K\lambda/(\beta cos\theta) \quad (1)$$

In the equation, d is the average diameter of the grains, K is constant 0.89, β is the half-height width of the diffraction peak of the sample, λ is X-ray wavelength of 1.54056 nm, θ is the Bragg angle corresponding to the diffraction peak. As shown in Table 1, crystallite sizes of pure ZnO, $ZnSnO_3$/ZnO, and Bi_2MoO_6/$ZnSnO_3$/ZnO are 40.03 nm, 35.35 nm, and 10.65 nm, respectively, showing a decreasing trend. Due to the stronger binding force of $ZnSnO_3$ and ZnO, the crystallite size of $ZnSnO_3$/ZnO and Bi_2MoO_6/$ZnSnO_3$/ZnO composites decreased compared to that of pure ZnO. Furthermore, the composites are not destroyed by secondary hydrothermal effect after the Bi_2MoO_6 loading. Meanwhile, the crystallite size of the composites becomes small because the temperature programming device is characterized by fast and uniform heating, and the uniform temperature distribution within the crystal ensures uniform crystallite distribution.

3.2 SEM–EDS

To investigate the morphological features and elemental distribution of the composites, SEM analysis and EDS analysis were performed on Bi_2MoO_6/$ZnSnO_3$/ZnO composite. Figure 2a–d are scanning electron microscope (SEM) images of different materials, where the monomeric ZnO exhibits a rod-like structure with a diameter of about 400 nm (Fig. 2a). The $ZnSnO_3$/ZnO material synthesized by the hydrothermal method exhibits a cubic structure with heterogeneous particles attached to the surface (Fig. 2b). After secondary hydrothermal treatment, the morphology of Bi_2MoO_6/$ZnSnO_3$/ZnO composite in Fig. 2c does not change much compared with $ZnSnO_3$/ZnO, indicating that secondary hydrothermal did not affect the morphology of the composite. It can be found from the figure that the morphological size of the composites is around 1 μm. Figure 2e–i show the EDS elemental analysis of the composites in the range of Fig. 2d, from which it can be found that all elements are evenly distributed. The analysis of the contents of each element in the composites is shown in Fig. 2j.

Table 1 Crystallite sizes (d), band gap energy values (Eg), BET specific surface area (S_{BET}), average pore diameter (D) and pore volume (V_{total}) of different samples

Sample	d (nm)	Eg (eV)	S_{BET} ($m^2\ g^{-1}$)	D (nm)	V_{total} ($cm^3\ g^{-1}$)
ZnO	40.03	3.24	7.24	2.9	0.0143
$ZnSnO_3$/ZnO	35.35	3.02	15.58	3.2	0.0216
Bi_2MoO_6/$ZnSnO_3$/ZnO	10.65	2.83	21.03	4.23	0.0633

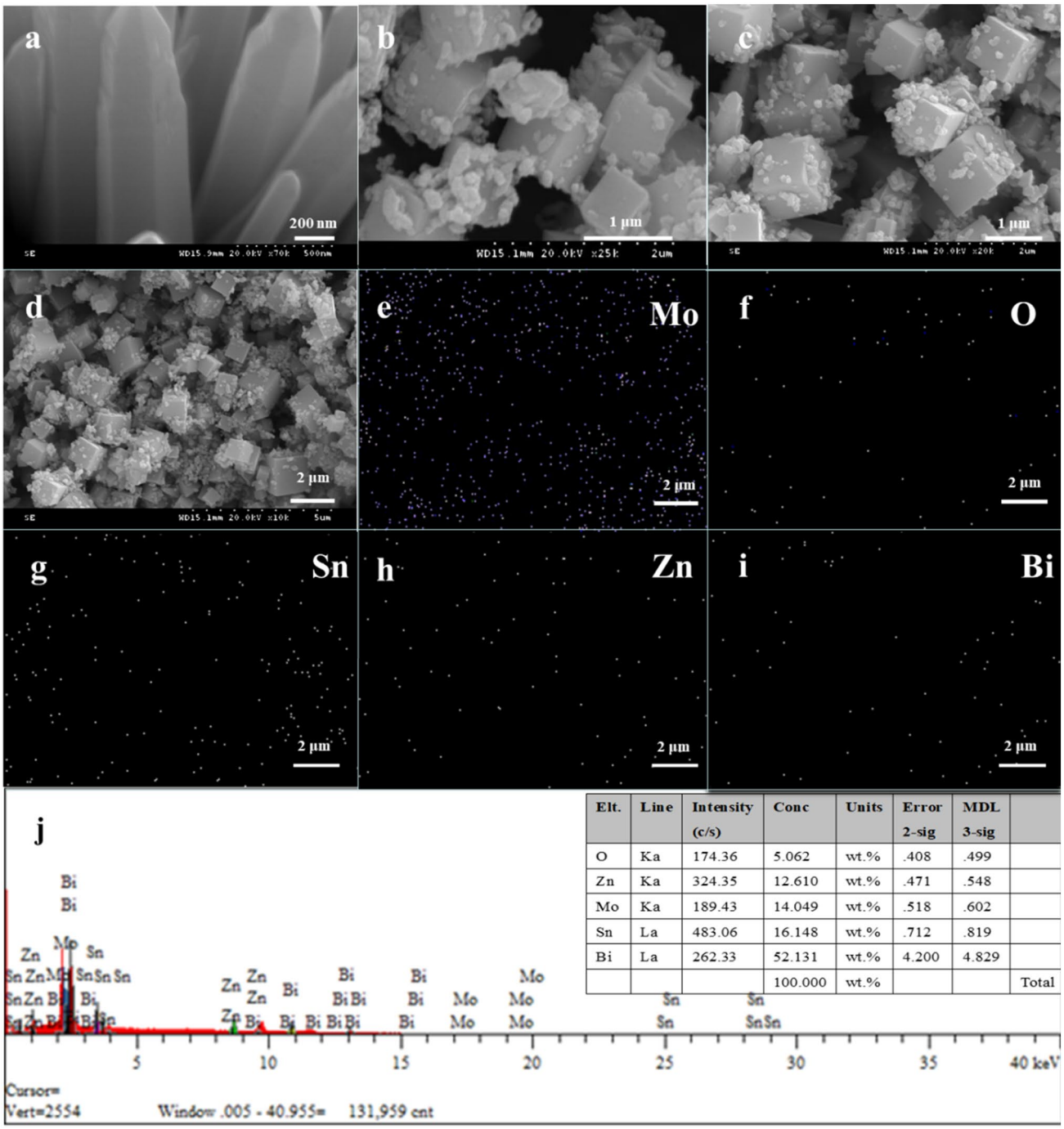

Fig. 2 SEM images of ZnO (**a**), $ZnSnO_3$/ZnO (**b**), Bi_2MoO_6/$ZnSnO_3$/ZnO (**c**) and EDS images of Bi_2MoO_6/$ZnSnO_3$/ZnO composite (**d**)–(**i**), EDS of each element in the composite (**j**)

3.3 TEM and HR-TEM

To further investigate the morphology of the Bi_2MoO_6/$ZnSnO_3$/ZnO composite, TEM and high-resolution transmission electron microscopy (HR-TEM) analyses were performed. TEM images of the composites are shown in Fig. 3a, from which the composites exhibit a solid structure. Through the HR-TEM images (b–f) of the composite, it can be seen that the lattice spacing of 0.28 nm corresponds to the (100) crystal plane of ZnO [31], the lattice spacing of 0.31 nm corresponds to the (131) crystal plane of Bi_2MoO_6 [32], and the lattice spacing of 0.23 nm corresponds to the (200) crystal plane of $ZnSnO_3$ [33].

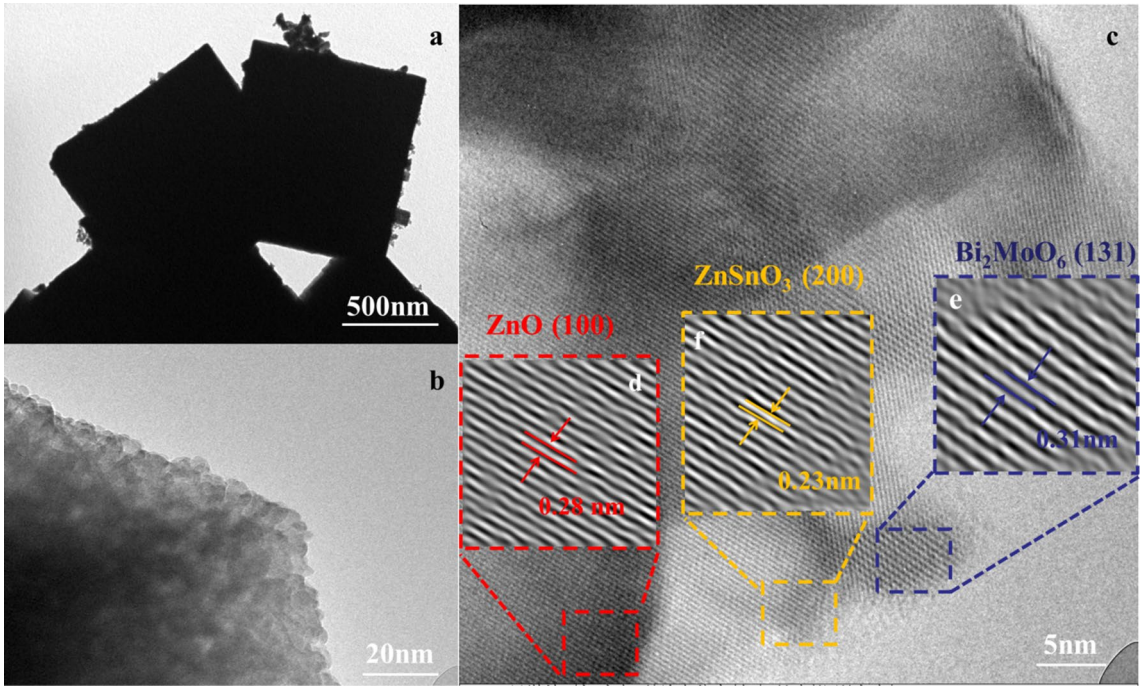

Fig. 3 TEM image (**a**), and HR-TEM images of the $Bi_2MoO_6/ZnSnO_3/ZnO$ composite (**b**, **c**)

The above results indicate that in the as-synthesized $Bi_2MoO_6/ZnSnO_3/ZnO$ composites, tight junctions were formed between $ZnSnO_3$ and ZnO, thus forming heterojunctions, which are beneficial to enhance the separation rate of photogenerated carriers and thus enhance the separation efficiency of photogenerated electron hole pairs. Moreover, because the Bi_2MoO_6 has a more negative conduction band potential than ZnO, it can significantly inhibit the rapid recombination of photogenerated carriers inside ZnO, and improve the lifetime of photogenerated carriers in the composites.

3.4 XPS analysis

X-ray photoelectron spectroscopy (XPS) was used to analyze the chemical form of the surface element of the composite $Bi_2MoO_6/ZnSnO_3/ZnO$. Figure 4a shows that the peaks correspond to five elements, including Zn, Bi, O, Mo, and Sn. Two characteristic peaks at 1043.72 and 1020.37 eV of electron binding energy in Fig. 4b correspond to Zn $2p_{3/2}$ and Zn $2p_{1/2}$, proving that the Zn element exists Zn^{2+} form [13]. Figure 4c shows that two strong peaks at 158.16 and 163.46 eV appear in the Bi 4f region, illustrating that Bi exists in the Bi^{3+} form [34, 35]. Figure 4d shows the XPS spectrum of O at O1s in the composite $Bi_2MoO_6/ZnSnO_3/ZnO$ with electron binding energy region at 528.8 eV, 529.79 eV, and 531.03 eV, corresponding to the characteristic peaks of lattice oxygen (Zn–O) and adsorbed oxygen [36]. The peaks at binding energies of 231.01 eV and 234.47 eV (Fig. 4e) correspond to Mo $3d_{5/2}$ and Mo $3d_{3/2}$ of Mo^{6+} in Bi_2MoO_6, respectively [37]. In Fig. 4e, the peak at the binding energy of 232.2 eV may result from the oxygen vacancy generation in the composites, and the electronic reconstruction between chemical bonds changes the valence state of Mo [37]. The binding energy peaks at 485.43 and 494.29 eV in Fig. 4f correspond to Sn $3d_{3/2}$ and Sn $3d_{5/2}$ of Sn^{4+}, respectively [38]. The above results can further demonstrate the existence of each species in the composite $Bi_2MoO_6/ZnSnO_3/ZnO$.

3.5 N_2 Adsorption–Desorption Analysis

The surface area can usually impact the adsorption and catalytic performance of photocatalysts. In order to investigate the surface physicochemical characteristics of the $Bi_2MoO_6/ZnSnO_3/ZnO$ composite, nitrogen adsorption–desorption isotherms were used to characterize ZnO, $ZnSnO_3/ZnO$, and $Bi_2MoO_6/ZnSnO_3/ZnO$ composite. Figure S1 and Table 1 show that the $Bi_2MoO_6/ZnSnO_3/ZnO$ composite exhibits a larger specific surface area than pure ZnO. The IUPAC definition shows that isotherms of each sample in Fig. S1 are of type IV, indicating that the different samples prepared all have a mesoporous structure. The above materials have the same type of hysteresis loop as the H3 type hysteresis loop. The formation of this hysteresis loop is mainly due to the capillary condensation phenomenon in mesopores. The inset of Fig. S1 shows the pore size distribution curve of each material. The pore size distribution of ZnO and $ZnSnO_3/ZnO$ is relatively concentrated, while that

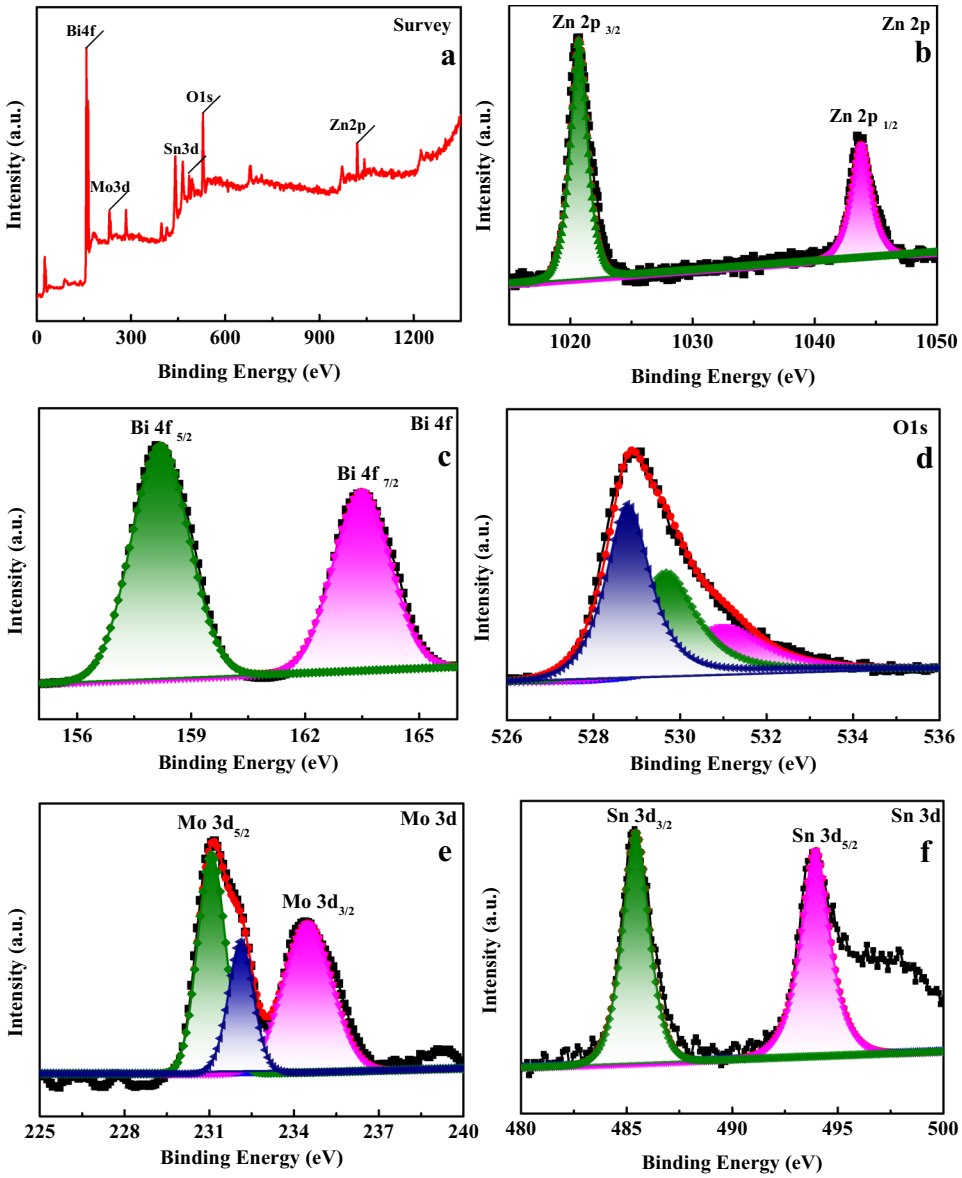

Fig. 4 XPS spectra of Bi_2MoO_6/$ZnSnO_3$/ZnO composite: **a** XPS full spectrum, **b** Zn 2p, **c** Bi 4f, **d** O 1s, **e** Mo 3d, **f** Sn 3d

of Bi_2MoO_6/$ZnSnO_3$/ZnO composites is relatively broad. Table 1 shows that the average pore size, specific surface area, and pore volume of Bi_2MoO_6/$ZnSnO_3$/ZnO composites are larger than those of monomeric ZnO and $ZnSnO_3$/ZnO, and the pore size distribution is better than that of monomeric ZnO and $ZnSnO_3$/ZnO, indicating that the composite after loading Bi_2MoO_6 can both effectively improve the specific surface area of the catalysts and optimize the pore size distribution, thereby reducing the substance diffusion resistance. Therefore, it is beneficial to improve the photocatalytic activity of the composite.

3.6 UV–Vis/DRS Analysis

In order to determine whether the samples have the absorption in the ultraviolet and visible regions, the results of the UV–Vis diffuse reflectance were exhibited in Fig. 5. The absorption spectra of different catalysts are shown in Fig. 5a. The Kubelka–Munk energy plots for different samples are shown in Fig. 5b. Figure 5a shows that the absorption edge of ZnO is around 400 nm due to its wide band gap value. In contrast, pure Bi_2MoO_6 has an absorption edge at approximately 500 nm, consistent with previous reports showing light absorption in UV light and visible light regions. Besides, the visible light absorption ability of $ZnSnO_3$/ZnO composites is improved compared with ZnO. Since Bi_2MoO_6 has visible light absorption, the light absorption band edge of the composites is red-shifted with about 90 nm after loading of Bi_2MoO_6.

Equation 2 is used to determine the nature of transition and obtain the band gap of the sample.

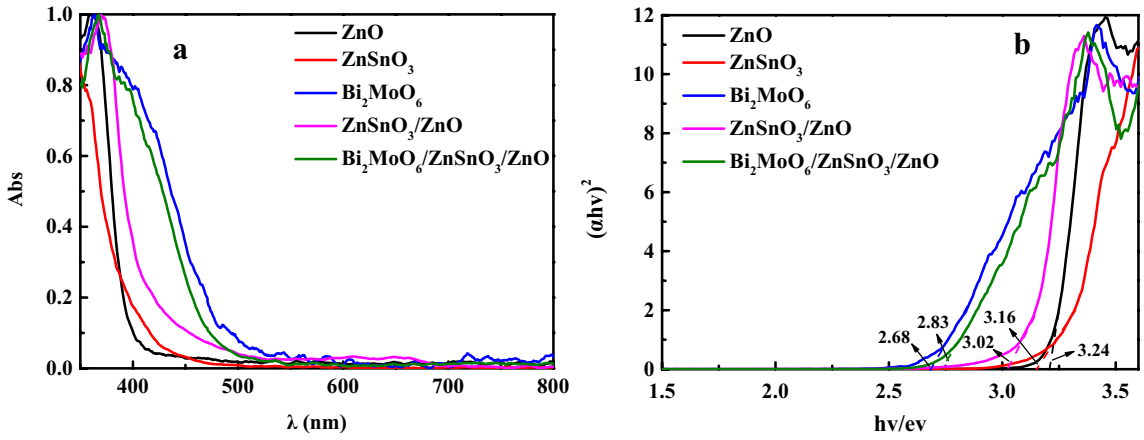

Fig. 5 The **a** UV–Vis/DRS absorption spectra and **b** Kubelka–Munk energy curve plots for different samples

$$\alpha h\nu = A \cdot (h\nu - Eg)^{n/2} \quad (2)$$

where α, $h\nu$, and A are the absorption coefficient, discrete photon energy, and constant. Besides, the value of n is determined by the type of optical transition in the semiconductor (n = 1 for direct transition and n = 4 for indirect transition). Since both ZnO and Bi_2MoO_6 belong to indirect transition semiconductors, their n values are both 4. The $(\alpha h\nu)^2$ and $h\nu$ curves of ZnO and Bi_2MoO_6 are shown in Fig. 5b. The band gap values of ZnO and Bi_2MoO_6 are about 3.24 eV and 2.68 eV, close to the values reported previously. The tangent treatment to the Kubelka–Munk energy curve shows that band gap values of $ZnSnO_3$/ZnO, and Bi_2MoO_6/$ZnSnO_3$/ZnO composites are 3.02 eV and 2.83 eV, respectively. After the successful loading of Bi_2MoO_6, the band gap values of the composites are further reduced. The above results illustrate that Bi_2MoO_6 is successfully loaded on $ZnSnO_3$/ZnO, further reducing the band gap of the composites. Besides, Bi_2MoO_6 is expected to improve the photocatalytic activity of the composites.

3.7 Photoelectrochemical Performance

The transfer and recombination of the photoinduced electron hole pairs in the photocatalytic materials were investigated by performing PL, EIS and transient photocurrent analysis of the composites. The photoluminescence (PL) test was performed by exciting the Bi_2MoO_6/$ZnSnO_3$/ZnO composite with 500 nm light. Generally, a PL emission signal arises from the recombination of charge carriers in a semiconductor. A lower PL emission intensity indicates a lower electron–hole pair recombination which facilitates a photocatalytic reaction [39]. As shown in Fig. S2, PL intensity is ZnO > $ZnSnO_3$/ZnO > Bi_2MoO_6/$ZnSnO_3$/ZnO, and Bi_2MoO_6/$ZnSnO_3$/ZnO exhibits the lowest luminescence intensity, indicating that it has the lowest electron hole recombination rate. This result suggests that the fabrication of the ternary heterojunction can effectively reduce electron–hole recombination, which is essential in the enhancement of photocatalytic activity.

EIS was used to determine the charge transfer resistance of the materials [40]. A smaller arc radius in the EIS Nyquist plot indicated a lower charge transfer resistance at the interface between the electrode and the electrolyte solution, implying a better migration of the charge carrier. The Nyquist curves of different samples are shown in the Fig. 6a, the arc radius of Bi_2MoO_6/$ZnSnO_3$/ZnO composite is smaller than that of $ZnSnO_3$/ZnO and ZnO, indicating that Bi_2MoO_6/$ZnSnO_3$/ZnO composite has the highest level of effective charge transfer efficiency. Therefore, a large number of charge carriers participate in the photocatalytic reaction [41]. Figure 6b shows the transient photocurrent responses of ZnO, $ZnSnO_3$/ZnO, and Bi_2MoO_6/$ZnSnO_3$/ZnO composites during several cycles of switching on and off visible light illumination. The photocurrent intensity increases rapidly when the visible light is turned on and decreases directly when the visible light is turned off. Among other photocatalysts, Bi_2MoO_6/$ZnSnO_3$/ZnO exhibits the strongest photocurrent response, indicating that it had a high ability to generate and transfer photoactivated charge carriers. In combining the PL, EIS, and photocurrent responses results, the interfacial charge transfer efficiency in Bi_2MoO_6/$ZnSnO_3$/ZnO was greatly enhanced when compared with ZnO and $ZnSnO_3$/ZnO, which is occurred as a result of the formation of multi-heterojunctions [42]. This heterojunction structure can effectively suppress charge recombination in the composite material and thus has a higher photocatalytic response.

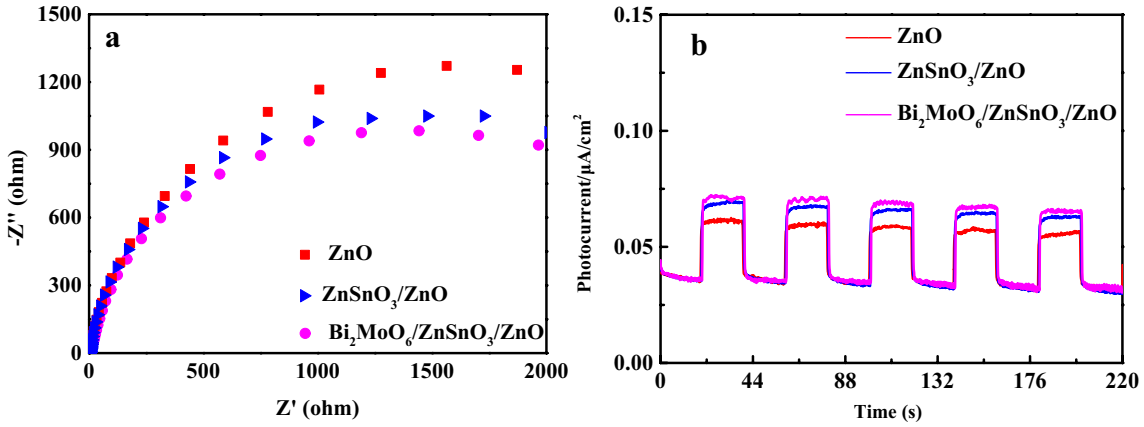

Fig. 6 EIS Nyquist plots (**a**) and transient photocurrent response analysis (**b**) of different composites

3.8 Photocatalytic Performance

In order to investigate the practical application ability of the synthesized composite materials, the photocatalytic performance of the composites was analyzed by performing multi-modal photocatalytic experiments under UV, visible and simulated solar light, as shown in Fig. 7. Within identical experimental conditions, the degradation efficiency of $Bi_2MoO_6/ZnSnO_3/ZnO$ composite to CV under UV light irradiation can reach 90% within 120 min. The composite shows the best degradation effect on CV under UV light. Therefore, CV is chosen as the model molecule in this paper. The composites degrade other dyes and tetracycline hydrochloride under UV light irradiation, as shown in Fig. 7c, indicating that the composites can degrade different organic pollutants. In order to further investigate the effect of the $Bi_2MoO_6/ZnSnO_3/ZnO$ catalyst on the CV degradation, the photodegradation activity of pure ZnO, Bi_2MoO_6, $ZnSnO_3$/ZnO, and $Bi_2MoO_6/ZnSnO_3/ZnO$ was examined under ultraviolet light irradiation. In Fig. 7a, in the control system without photocatalyst, the CV dye hardly decomposes, which proves that the degradation is driven by photocatalysis [43]. The photocatalytic activity of $Bi_2MoO_6/ZnSnO_3/ZnO$ under UV light irradiation is higher than that of the other samples, and the photocatalytic efficiency is 1.8 times that of monomeric ZnO and 1.2 times that of $ZnSnO_3$/ZnO, whose photocatalytic efficiency is significantly improved, consistent with the results of UV–Vis diffuse reflectance absorption spectra. The UV–Vis spectra of CV at different degradation times with 0.15 g $Bi_2MoO_6/ZnSnO_3/ZnO$ (CV concentration of 50 mg L^{-1}) is shown in Fig. S3.

In order to investigate the reaction kinetics of the photocatalytic degradation of CV by ZnO, Bi_2MoO_6, $ZnSnO_3$/ZnO and $Bi_2MoO_6/ZnSnO_3/ZnO$, the Langmuir Hinshelwood equation (Eq. 3) is fitted to the experimental data in Fig. 7a:

$$ln(C_0/C_t) = Kappt \tag{3}$$

where C_0, C_t are the initial and residual concentrations of CV in the reaction mixture (mg L^{-1}), Kapp is the pseudo-first-order rate constant for photocatalytic degradation (min^{-1}), t is the time (min), and the linear fitted curve with irradiation time is shown in Fig. 7b.

Figure 7b shows that $ln(C_0/C_t)$ has a linear relationship with the reaction time t, indicating that the degradation of dye molecules follows the pseudo-first-order reaction kinetics. The photocatalytic activity of the $Bi_2MoO_6/ZnSnO_3$/ZnO composite is determined by testing its activity in the degradation of CV under visible light and simulated sunlight, as shown in Fig. 7d and e. $Bi_2MoO_6/ZnSnO_3/ZnO$ exhibits the optimal photocatalytic degradation efficiency within visible and simulated daylight irradiation. In general, the photocatalytic activity of a photocatalyst depends on various factors such as photogenerated electron–hole pair migration rate, light absorption ability and specific surface area. Combined with the above test results, it is clearly found that the special introduction of $ZnSnO_3$ can further improve the photocatalytic activity, which may be caused by its superior crystal form and morphology structure. After Bi_2MoO_6 was further successfully loaded, due to its excellent absorption in the visible region and the successful construction of heterostructures between components, the utilization of visible light of the composite was significantly improved. At the same time, the rapid recombination of photogenerated electron and hole pairs in the composites has been effectively inhibited, and the ability to generate and transfer photoactivated charge carriers has been further enhanced. Therefore, the photocatalytic activity of the composites has been significantly further improved.

In order to explore the main active molecules in the process of photocatalytic reaction, trapping experiments are performed, as shown in Fig. 8. Under the same experimental

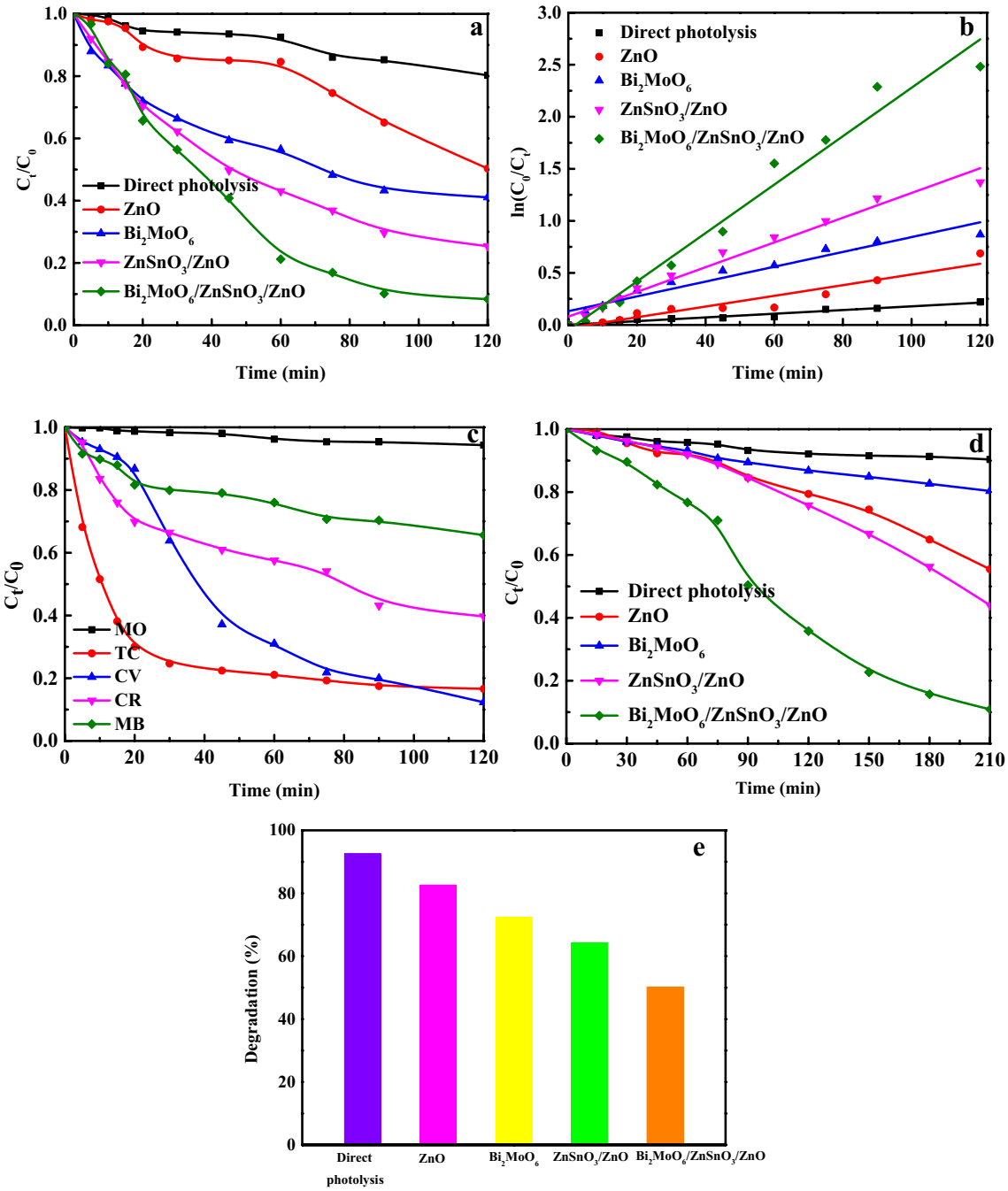

Fig. 7 **a** Degradation of CV by different catalysts under ultraviolet light (t = 120 min), **b** corresponding pseudo first order kinetic fitting curves of different catalysts under UV light irradiation, **c** experimental results of degradation of different organic pollutants by Bi_2MoO_6/$ZnSnO_3$/ZnO under ultraviolet light, **d** degradation of CV by different catalysts under visible light (t = 210 min), **e** degradation of CV by different catalysts under simulated sunlight (t = 300 min)

conditions, superoxide radical ($\cdot O_2^-$), hydroxyl radical ($\cdot OH^-$) and hole (h^+) [44] were trapped by adding p-benzoquinone (BQ), isopropanol (IPA) and disodium ethylenediaminetetraacetate (EDTA-2Na) under UV light irradiation, respectively, to get the capture experimental results.

Figure 8 shows that the degradation efficiency of CV appeared obviously different after different trapping agents were added under UV light irradiation. Among them, the degradation efficiency of CV is suppressed after adding isopropanol (IPA) and disodium ethylenediaminetetraacetic acid (EDTA-2Na), indicating that the main active species

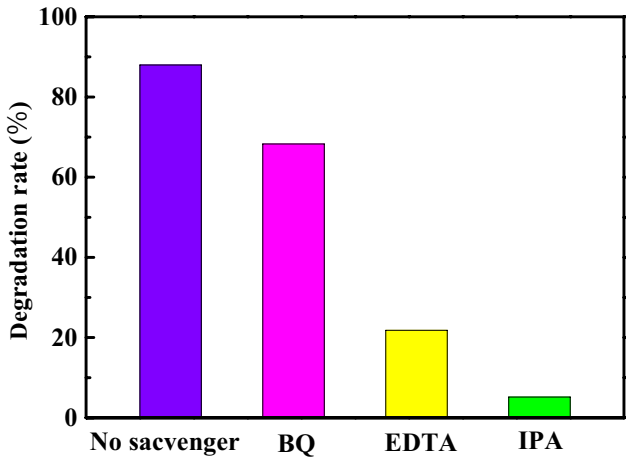

Fig. 8 Capture experimental results of $Bi_2MoO_6/ZnSnO_3/ZnO$ under UV light

in the photodegradation of CV by the $Bi_2MoO_6/ZnSnO_3/ZnO$ composite are hydroxyl radicals ($\cdot OH^-$) and holes (h^+), while superoxide radicals ($\cdot O_2^-$) plays a certain auxiliary role.

In order to investigate the stability of the composite, $Bi_2MoO_6/ZnSnO_3/ZnO$ is subjected to three cycling degradation tests under UV irradiation, as shown in Fig. S4. After three-cycle tests, the $Bi_2MoO_6/ZnSnO_3/ZnO$ composite still has good photocatalytic degradation activity, indicating that the composite shows good stability.

3.9 LC–MS Analysis

In order to further explore the reaction mechanism of CV degradation by composite, 1 mL is sampled every 30 min interval by LC–MS to identify the intermediates of the reaction, and the possible degradation pathways of the corresponding intermediates and CV on $Bi_2MoO_6/ZnSnO_3/ZnO$ are proposed [45, 46], as shown in Fig. 9.

The comparison between the assay results and the standard database shows that the resulting degradation intermediates mainly consist of components (i), (ii), (iii), (iv), (v), (vi), (vii), (viii), etc. According to the above results and some previous reports, the possible photocatalytic degradation pathways of $Bi_2MoO_6/ZnSnO_3/ZnO$ can be further inferred, as shown in Fig. 9.

Hydroxyl radicals and metal cations attack the CV in the oxidized lattice formed on the surface of $Bi_2MoO_6/ZnSnO_3/ZnO$ composites, and the chemical names and molecular formulas of the generated components are shown in Table S1. Finally, hydroxyl radicals promote oxidative ring opening reactions to generate some simpler small molecule compounds, which are finally converted to H_2O, CO_2, and inorganic ions.

3.10 Possible Photocatalytic Reaction Mechanism

To explore the migration path of photogenerated carriers in the composite photocatalysts $Bi_2MoO_6/ZnSnO_3/ZnO$, the positions of the energy bands are calculated using Eqs. (4) and (5), as shown in Table 2.

$$E_{CB} = \chi - E_C - 0.5 \cdot E_g \tag{4}$$

$$E_{VB} = E_{CB} + E_g \tag{5}$$

In these formulas, X is the absolute value of the absolute electronegativity of the semiconductor photocatalyst. E_c is the standard hydrogen electrode potential (4.5 eV). E_{VB} and E_{CB} are the energy band positions of valence and conduction bands of composites, respectively, and Eg is the band gap value of the semiconductor.

The possible photocatalytic mechanism of the $Bi_2MoO_6/ZnSnO_3/ZnO$ composites is speculated from the above calculation results and the trapping experiment results, as shown in Fig. 10.

During the synthesis of the composites, heterojunctions were formed due to the matching of energy bands. Under simulated sunlight irradiation, the components in the $Bi_2MoO_6/ZnSnO_3/ZnO$ composites absorb the ultraviolet light component in simulated daylight. Therefore, the photogenerated electrons are excited from the valence band (VB) to its conduction band of the composites (CB), and the same number of holes are retained in the VB. Only electrons at the conduction band of ZnO react with dissolved oxygen to generate superoxide radical ($\cdot O_2^-$) and holes (h^+) at the valence band of Bi_2MoO_6 react with water molecules to generate hydroxyl radical ($\cdot OH^-$). ($\cdot O_2^-$), ($\cdot OH^-$) and h^+ react with organic pollutants to generate carbon dioxide (CO_2), water (H_2O) and inorganic ions, respectively, and then successfully degrade pollutants.

4 Conclusions

In summary, a double Z-type heterojunction photocatalyst $Bi_2MoO_6/ZnSnO_3/ZnO$ with visible light response was successfully synthesized for the first time in this experiment through a simple hydrothermal pathway, and the degradation of CV and antibiotics were effectively investigated as simulated pollutants. Due to the existence of different energy levels, photogenerated electrons and holes can migrate between different materials. The double Z-type heterojunction formed between ZnO, $ZnSnO_3$ and Bi_2MoO_6 greatly further optimizes the charge transfer path, prolongs the lifetime of photogenerated carriers, effectively improves the charge separation efficiency, and then greatly improves the photocatalytic activity of the composites. It is proved that

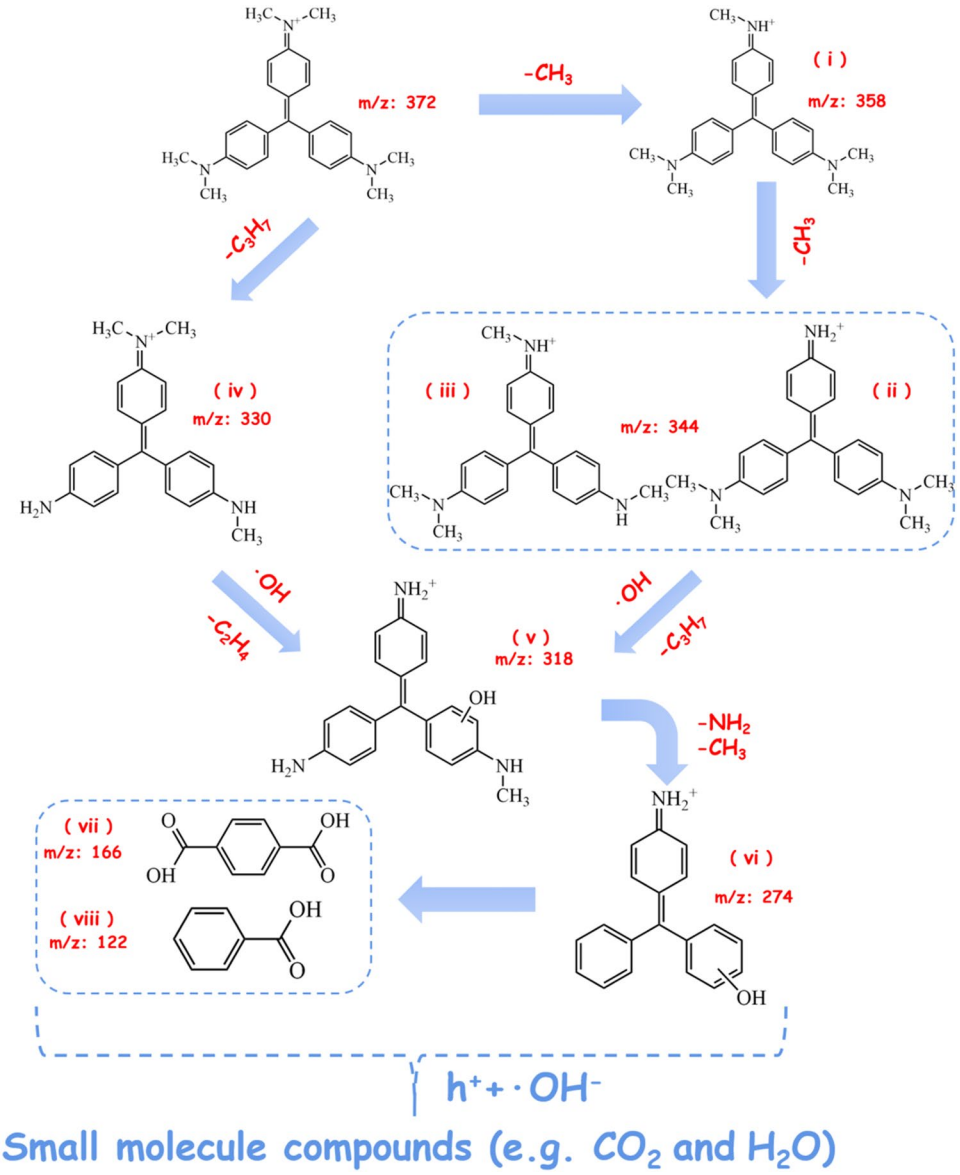

Fig. 9 Degradation pathway of CV on Bi_2MoO_6/$ZnSnO_3$/ZnO composite under UV light irradiation

Table 2 Absolute electronegativity (χ), band gap energy (Eg), conduction band (CB), valence band (VB) of ZnO, $ZnSnO_3$, and Bi_2MoO_6

Semiconductor	χ (eV)	Eg (eV)	E_{CB} (eV)	E_{VB} (eV)
ZnO	5.79	3.24	− 0.33	2.91
$ZnSnO_3$	6.06	3.16	− 0.002	3.14
Bi_2MoO_6	6.31	2.68	0.47	3.15

the composite catalyst has superior photocatalytic activity than monomer and binary catalyst, and $\cdot OH^-$ and h^+ play a major role in the photocatalytic system. At the same time, the degradation mechanism was described in detail through the intermediate products in the degradation process of CV. In a word, the successful preparation of the double Z-type

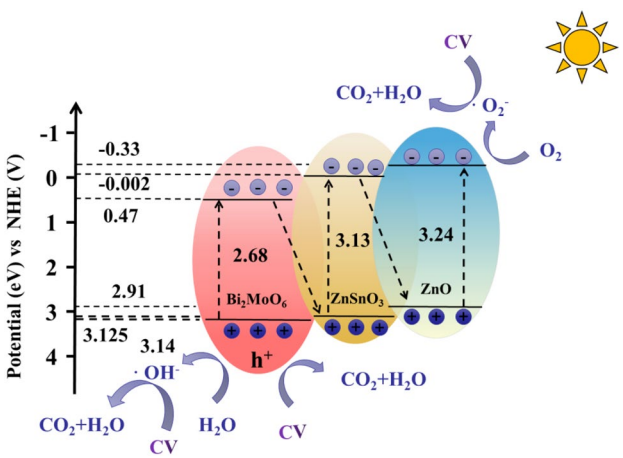

Fig. 10 Possible photocatalytic reaction mechanism of Bi_2MoO_6/$ZnSnO_3$/ZnO under simulated sunlight irradiation

heterojunction photocatalyst $Bi_2MoO_6/ZnSnO_3/ZnO$ provides a new photocatalytic material and structural technology for high-efficiency photocatalytic degradation of refractory organic wastewater, and greatly expands the application of ZnO based double Z-type heterojunction photocatalyst in the field of photocatalysis.

Supplementary Information The online version contains supplementary material available at https://doi.org/10.1007/s10904-022-02242-y.

Acknowledgements This study was supported by the National Natural Science Foundation of China (Grant Nos. 21776144, 21376126), the Heilongjiang Provincial Natural Science Foundation of China (Grant No. LH2021B031), the Fundamental Research Funds in Heilongjiang Provincial Universities of China (Grant No. 145109104), the Innovation Project of Qiqihar University Graduate Education (Grant No. YJSCX2020037), and the College Students' Innovative Entrepreneurial Training Program Funded Projects of Qiqihar University (Grant No. 202110232154).

Author Contributions The first draft of the manuscript was written by YG and revised by LL and all authors commented on previous versions of the manuscript. Material preparation, data collection and analysis were performed by YG, LL, WZ and YS. Technical support and supervision of instrument operation were provided by YC and WZ. Manuscript preservation and visualization were provided by GJ and YH.

Funding This work was supported by [the National Natural Science Foundation of China, the Heilongjiang Provincial Natural Science Foundation of China, the Fundamental Research Funds in Heilongjiang Provincial Universities of China, the Innovation Project of Qiqihar University Graduate Education and the College Students' Innovative Entrepreneurial Training Program Funded Projects of Qiqihar University] (Grant Numbers [21776144, 21376126] and [LH2021B031] and [145109104] and [YJSCX2020037] and [202110232154]).

Data Availability The datasets generated during and/or analyzed during the current study are available from the corresponding author on reasonable request

Declarations

Conflict of interest The authors have no relevant financial or non-financial interests to disclose.

References

1. P. Zhu, J. Xu, M. Duan, R. Wang, L. Xie, M. Hu, P. Wang, Opt. Mater. **107**, 110076 (2020)
2. M. Pirhashemi, A. Habibi-Yangjeh, Mater. Chem. Phys. **214**, 107 (2018)
3. P. Gul, K.S. Ahmad, S.B. Jaffri, D. Ali, Soil Sediment Contam. **30**, 9798 (2021)
4. A.A. Walied, H.T. Mohamed, Handal, J. Hazard. Mater. **404**, 123946 (2021)
5. J. Singh, S. Kumar, A.K. Rishikesh, R.K. Manna, Soni, Opt. Mater. **107**, 110138 (2020)
6. T. Kanagaraj, S. Thiripuranthagan, S.M.K. Paskalis, H. Abe, Appl. Surf. Sci. **426**, 1030 (2017)
7. M.K. Singha, A. Patra, Opt. Mater. **107**, 110000 (2020)
8. M. Kasinathan, S. Thiripuranthagan, A. Sivakumar, S. Ranganathan, T. Vembuli, S. Kumaravel, E. Erusappan, Mater. Res. Bull. **125**, 110782 (2020)
9. B. Appavu, S. Thiripuranthagan, S. Ranganathan, E. Erusappan, K. Kannan, Ecotoxicol. Environ. Saf. **151**, 118 (2018)
10. H.J. Jung, R. Koutavarapu, S. Lee, J.H. Kim, H.C. Choi, M.Y. Choi, J. Alloys Compd. **735**, 2058 (2018)
11. A. Rafiq, M. Ikram, S. Ali, F. Niaz, J. Ind. Eng. Chem. **97**, 111 (2021)
12. C.N. Ri, S.G. Kim, K.S. Ju, H.-S. Ryo, C.H. Mun, U.H. Kim, RSC Adv. **8**, 5433 (2018)
13. K. Omri, S. Gouadria, J. Mater. Sci. Mater. Electron. **32**, 17021 (2021)
14. K. Omri, I. Najeh, L.El Mir, Ceram. Int. **42**, 8940 (2016)
15. B. Gao, M. Sun, W. Ding et al., Appl. Catal. B **281**, 119492 (2021)
16. K. Omri, F. Alharbi, J. Mater. Sci.: Mater. Electron. **32**, 24229 (2021)
17. K. Omri, A. Bettaibi, K. Khirouni, L. El Mir, Phys. B Condens. Matter. **537**, 167 (2018)
18. T. Di, Q. Xu, W. Ho, H. Tang, Q. Xiang, J. Yu, ChemCatChem. **11**, 1394 (2019)
19. W.-K. Jo, T. Adinaveen, J.J. Vijaya, N.C.S. Selvam, RSC Adv. **6**, 10487 (2016)
20. Q.J. Liu, H. Qin, Z. Jiao, F.S. Liu, Z.T. Liu, Mater. Chem. Phys. **180**, 75 (2016)
21. P. Luo, H.J. Zhang, L. Liu, L. Fang, Y. Wang, Electrochim. Acta **219**, 734 (2016)
22. S. Dong, J. Sun, Y. Li, C. Yu, Y. Li, J. Sun, Appl. Catal. B Environ. **144**, 386 (2014)
23. G. Wang, Y. Xi, H. Xuan, R. Liu, X. Chen, L. Cheng, Nano Energy **18**, 28 (2015)
24. H. Xu, Y. Huang, D. Luo, X. Yang, S. Jin, Q. Guo, Y. Zhao, Y. Fang, Y. Wei, J. Wu, Separ. Purif. Technol. **210**, 281 (2019)
25. S. Yu, X. Jia, J. Yang, S. Wang, Y. Li, H. Song, Mater. Lett. **291**, 129531 (2021)
26. D. Lian, B. Shi, R. Dai, X. Jia, X. Wu, J. Nanopart. Res. **19**, 401 (2017)
27. S. Adhikari, S. Selvaraj, D.H. Kim, Appl. Catal. B **244**, 11 (2019)
28. Y. Yan, J. Liu, H. Zhang, D. Song, J. Li, P. Yang, M. Zhang, J. Wang, J. Alloys Compd. **780**, 193 (2019)
29. Y. Peng, Y. Zhang, F. Tian, J. Zhang, J. Yu, Solid State Mater. **8436**, 1 (2017)
30. J. Low, C. Jiang, B. Cheng, S. Wageh, A.A. Al-Ghamdi, J. Yu, Small Methods **1**, 1700080 (2017)
31. M. Kasinathan, S. Thiripuranthagan, A. Sivakumar, Opt. Mater. **109**, 110218 (2020)
32. Y. Liu, Z.-H. Yang, P.-P. Song, R. Xu, H. Wang, Appl. Surf. Sci. **430**, 561 (2018)
33. L. Du, H. Zhang, M. Zhu, M. Zhang, Inorg. Chem. Front. **6**, 2311 (2019)
34. J.S. Raja, J. Clust. Sci. **102**, 1987 (2021)
35. D.J. Wang, H.D. Shen, L. Guo, C. Wang, F. Fu, Appl. Surf. Sci. **436**, 536 (2018)
36. C.H. Nguyen, M.L. Tran, T.T.V. Tran, R.-S. Juang, Sep. Purif. Technol. **232**, 115962 (2020)
37. G. Zhang, D. Chen, N. Li, Q. Xu, H. Li, J. He, J. Lu, Appl. Catal. B **250**, 313 (2019)
38. S.Y. Dong, L.F. Cui, W. Zhang, Chem. Eng. J. **384**, 123279 (2020)
39. H. Yu, B. Huang, H. Wang, X. Yuan, L. Jiang, Z. Wu, J. Zhang, G. Zeng, J. Colloid Interface Sci. **522**, 82 (2018)
40. S.R. Zhu, Q. Qi, W.N. Zhao, Y. Fang, L. Han, J. Phys. Chem. Solids **121**, 163 (2018)
41. M. Jiang, Y. Shi, J. Huang, L. Wang, H. She, Eur. J. Inorg. Chem. **2018**, 1834 (2018)
42. A. Chachvalvutikul, T. Luangwanta, S. Kaowphong, J. Colloid Interface Sci. **603**, 738 (2021)

43. X. Liu, Y. Wang, X.Y. Zhang, G.Q. .Xu, D.M. Wang, J. Hazard. Mater. **34**, 10 (2018)
44. J. Puneetha, N. Kottam, A. Rathna, Inorg. Chem. Commun. **125**, 1387 (2021)
45. S. Ben Ayed, M. Azam, S.I. Al-Resayes, F. Ayari, L. Rizzo, Catalyst **11**, 1358 (2021)
46. A. Chachvalvutikul, T. Luangwanta, S. Kaowphong, Nanomaterials **11**, 8 (2021)